

## Metasurface Hologram for Multi-Image Hiding and Seeking

Huan Zhao,<sup>1,2</sup> Chunmei Zhang,<sup>3</sup> Jinying Guo,<sup>2</sup> Shutian Liu,<sup>1,\*</sup> Xianzhong Chen,<sup>3,†</sup> and Yan Zhang<sup>1,2,‡</sup>

<sup>1</sup>*Department of Physics, Harbin Institute of Technology, Harbin, 150001, China*

<sup>2</sup>*Beijing Key Laboratory of Metamaterials and Devices, Key Laboratory of Terahertz Optoelectronics, Ministry of Education, Beijing Advanced Innovation Center for Imaging Theory and Technology, Department of Physics, Capital Normal University, Beijing, 100048, China*

<sup>3</sup>*Institute of Photonics and Quantum Sciences, School of Engineering and Physical Sciences, Heriot-Watt University, Edinburgh EH14 4AS, United Kingdom*


 (Received 15 April 2019; revised manuscript received 25 July 2019; published 5 November 2019)

Image encoding and decoding are significant for information security, authenticity verification, and anticounterfeiting. We propose and demonstrate a polarization multiplexed metasurface for multi-image hiding and seeking in the terahertz band. The designed metasurface is composed of rod slot antennas and C-shaped slot antennas operating for both linear and circular polarizations. Different hidden images are revealed by controlling the polarization states of the incident and detection light. Three channels for object image encoding are demonstrated, indicating that this approach can increase the degree of freedom for optical image hiding and verification. This work may open an alternative avenue for polarization-controlled metasurface design, product identification, optical image encoding, and optical information security.

DOI: [10.1103/PhysRevApplied.12.054011](https://doi.org/10.1103/PhysRevApplied.12.054011)

### I. INTRODUCTION

Image hiding and verification have been used in product identification, image encryption, and authenticity verification [1,2]. To increase the security of the identification system and allow users to access different encrypted content, multi-image hiding and verification in different channels are desirable. Metasurfaces are two-dimensional counterparts of metamaterials, which are typically composed of single-layer or few-layer stacks of subwavelength planar antennas. By tailoring the geometric parameters and the spatial distribution of the resonant antennas, the metasurfaces can modulate the phase, amplitude, and polarization of electromagnetic waves with operating wavelengths ranging from visible to microwave bands [3–7], leading to a plethora of metasurface devices with various functionalities [8–10]. Multiplexing methods have been employed to enrich the functionalities of metasurface devices. Almost all intrinsic physical properties of the electromagnetic wave, such as the wavelength, the temporal and spatial positions, and polarization state can be used as channels to carry and deliver information [11–15]. As one of fundamental properties of electromagnetic waves, polarization states contain valuable information.

An arbitrary polarization state can be expressed as the superposition of  $x$ - and  $y$ -polarizations in the linear polarization system or the superposition of left and right circular polarizations in the circular polarization system. The polarization state of the electromagnetic wave can be modulated by the anisotropy of asymmetric antennas [16–19], providing an alternative opportunity to develop multifunctional metasurface devices. Considerable effort has already been made to design polarization multiplexed metasurface devices such as metalenses [20–22], vortex beam generators [23–25], and metasurface holograms [26–28]. For example, Ye *et al.* demonstrated a spin- and wavelength-multiplexed hologram in the nonlinear regime based on the Pancharatnam-Berry (PB) phase of a U-shaped antenna [29]. Zhang *et al.* implemented an ultrathin optical device for simultaneous control of holograms and twisted light beams [30]. Although polarization multiplexed metasurface devices have been widely explored, a metasurface approach for simultaneous linear and circular polarization multiplexing for multi-image hiding and verification has not been demonstrated.

In this paper, we propose and experimentally demonstrate a single metasurface that can simultaneously control linearly and circularly polarized light beams for multi-image hiding and verification in the terahertz (THz) band. The metasurface is composed of two types of antennas, rod slot antennas and C-shaped slot antennas. The proposed metasurface can modulate the phase profile for linearly

\*stliu@hit.edu.cn

†x.chen@hw.ac.uk

‡yzhang@mail.cnu.edu.cn

polarized light and circularly polarized light, respectively. Unlike the previous work by Liu *et al.* [31], where the concept of the combined structures was used to design a C-shaped metasurface for the simultaneous control of phase and amplitude of converted linear polarized light, the combined structures here are designed and fabricated to develop a polarization multiplexed metasurface for multi-image hiding and seeking in the THz band. Furthermore, there is an interference between the waves from the rod slot antennas and that from the C-shaped slot antennas since the linear and circular bases are not orthogonal to each other, leading to the unique properties of the designed device consisting of the combined structures. The developed device has three channels to deliver optical information. By controlling the polarization states of the incident and detection waves, we can selectively exhibit the optical images hidden in three channels. The combination of rod slot antennas and C-shaped slot antennas can dramatically increase the capability of the metasurface devices for multi-image encoding and decoding. The uniqueness of the proposed approach may open an alternative avenue for optical image encoding and security of optical information.

## II. METHOD

To realize the polarization multiplexed functionality, the designed metasurface consists of rod slot antennas and C-shaped slot antennas, which can modulate the phase profiles for the incident light with linear and circular polarizations, respectively. The two polarization states can be expressed as follows:

$$\begin{aligned} \begin{bmatrix} \mathbf{E}_x \\ \mathbf{E}_y \end{bmatrix} &= \frac{1}{\sqrt{2}} \begin{bmatrix} 1 & 1 \\ -j & j \end{bmatrix} \begin{bmatrix} \mathbf{E}_L \\ \mathbf{E}_R \end{bmatrix}, \\ \begin{bmatrix} \mathbf{E}_L \\ \mathbf{E}_R \end{bmatrix} &= \frac{1}{\sqrt{2}} \begin{bmatrix} 1 & j \\ 1 & -j \end{bmatrix} \begin{bmatrix} \mathbf{E}_x \\ \mathbf{E}_y \end{bmatrix}. \end{aligned} \quad (1)$$

As shown in Fig. 1, the  $x$ -polarized light can excite the C-shaped slot antenna array, then it will be converted into the  $y$ -polarized light and generate a holographic letter “H” in channel 1 based on the gradient phase. Moreover, the  $x$ -polarized incident light can be considered as the superposition of the left and right circularly polarized light, so that it can also excite the rod slot antennas. The converted left circularly polarized (LCP) light generated by the interaction of the right circularly polarized (RCP) component with rod slot antennas will reconstruct a letter “C” in channel 2 and the converted RCP light generated by the

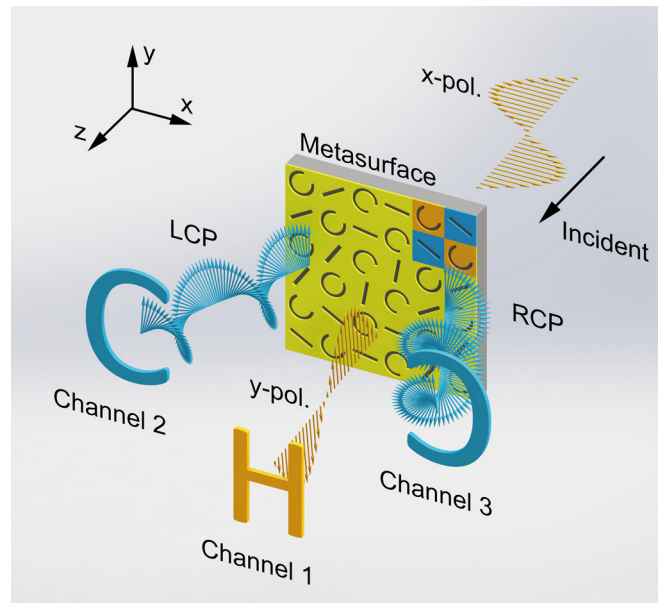


FIG. 1. Schematic diagram of a linear and circular polarization multiplexed metasurface for multi-image hiding and verification. The metasurface structure is composed of rod and C-shaped slot antennas. The holographic image of the letter “H” is hidden in channel 1, letter “C” in channel 2, and the mirror image of letter “C” in channel 3. Under the illumination of the  $x$ -polarized light, all three channels will be excited and under different detection polarization states, the information in different channels will be obtained.  $y$ -pol.,  $y$ -polarization;  $x$ -pol.,  $x$ -polarization; LCP, left-circular polarization; and RCP, right-circular polarization.

interaction of the LCP component with rod slot antennas will generate a mirror image of letter “C” in channel 3. If we detect the transmitted LCP light, we can obtain both the holographic letter “H” in channel 1 and the letter “C” in channel 2, that is, we cannot access the optical information in channel 3. We can select the polarization state of the incident and detection waves from four types:  $x$ -polarized,  $y$ -polarized, LCP, and RCP and different situations will appear on the imaging plane, which will be described in the Results and Discussion Section.

To improve the utilization efficiency, the rod slot and C-shaped antenna arrays are arranged like a checkerboard. The schematic of our design is shown in Fig. 2(a), where  $\varphi_1$  and  $\varphi_2$  represent the calculated phase modulation matrix of the rod slot antenna array and C-shaped slot antenna array, respectively.  $\varphi$  represents the final phase modulation distribution of the structure. The arrangement strategy can be expressed as

$$\varphi(x,y) = \begin{cases} \varphi_1(x,y), & x = 2n, y = 2m - 1 \text{ or } x = 2n - 1, y = 2m, \\ \varphi_2(x,y), & x = 2n - 1, y = 2m - 1 \text{ or } x = 2n, y = 2m, \end{cases} \quad (2)$$

where  $n$  and  $m$  are integer numbers ranging from 1 to 50.

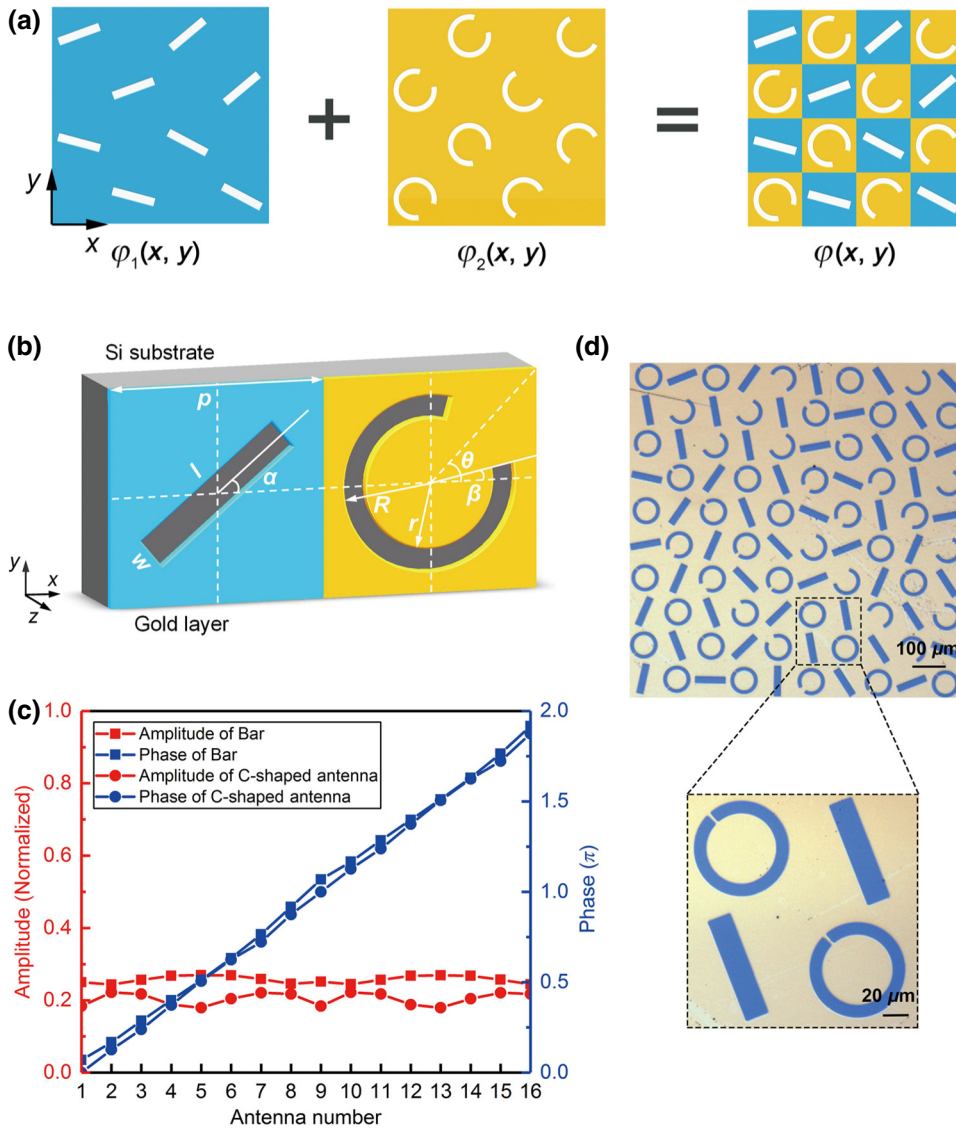


FIG. 2. Device design. (a) Schematic of the designed antennas.  $\varphi_1$ ,  $\varphi_2$  represent the calculated phase modulation matrix of the rod slot antenna array and C-shaped slot antenna array.  $\varphi$  represents the final phase modulation distribution of the structure. (b) Basic rod slot and C-shaped slot antenna. The period of both antennas  $P$  is  $100 \mu\text{m}$ .  $l$  and  $w$  are the length and width of the rod slot, which are  $90$  and  $20 \mu\text{m}$ , respectively.  $R$  and  $r$  are the outer and inner radii of the C-shaped slot, which are  $40$  and  $30 \mu\text{m}$ , respectively.  $\alpha$ ,  $\theta$  are the azimuthal angles of the rod slot antenna and C-shaped slot antenna.  $\beta$  is the opening angle of the split. (c) Simulated scattering amplitudes and phases of the cross-polarized radiation from the individual antenna units at  $0.8 \text{ THz}$ . The red and blue lines with square markers are the amplitude and phase modulation of the rod slot antennas, while the red and blue lines with circle markers are the amplitude and phase modulation of the C-shaped slot antennas. (d) Microscope image of the fabricated sample. The scale bars in the figure and inset are  $100$  and  $20 \mu\text{m}$ , respectively.

The building block is shown in Fig. 2(b). Each unit cell consists of a rod slot and a C-shaped slot, which are etched into a gold film with a thickness of  $0.1 \mu\text{m}$  sitting on a silicon substrate. The substrate is a  $500\text{-}\mu\text{m}$ -thick double-side polished high-resistivity silicon wafer, which has approximately  $70\%$  transmittance in the THz band. For the C-shaped slot antenna array, when a linearly polarized electromagnetic wave impinges on the antenna unit, both “symmetric” and “antisymmetric” modes can be excited and a cross-polarized field will be scattered by these two modes. The amplitude and phase of the reemitted field are modulated by adjusting the geometry parameters of the antennas. For the rod slot antennas, the orientation-dependent interaction with circularly polarized light generates the desired geometric phase discontinuity of  $\Phi = 2\sigma\alpha$  for the cross-polarized scattered field, where  $\sigma = \pm 1$  corresponds to the incident light with RCP and LCP and  $\alpha$  is the azimuthal angle of the rod slot antenna.

The parameters of the antennas are given in Fig. 2(b).  $P$  is the period of both antenna arrays, which is  $100 \mu\text{m}$ . The length  $l$  and width  $w$  of the rod slot are  $90$  and  $20 \mu\text{m}$ , respectively. The outer radius  $R$  and inner radius  $r$  of the C-shaped slot are  $40$  and  $30 \mu\text{m}$ , respectively. The azimuth angle  $\theta$  of the C-shaped slot is defined as the angle between the symmetric axis of the slot and the  $x$ -axis, and  $\beta$  is the open angle of the split. Sixteen rod slot antennas are selected to realize the phase modulation of a cross-circular-polarized wave ranging from  $0$  to  $2\pi$ , but with identical amplitude modulation at the operating frequency of  $0.8 \text{ THz}$  by changing the azimuth angle  $\alpha$ . Meanwhile,  $16$  C-shaped slot antennas are selected to realize the same modulation of the cross-linear-polarized wave by changing the opening angle  $\beta$ . By using these antennas, the phase modulation of the transmitted cross-polarized THz wave can reach  $2\pi$  with a constant phase difference of  $\pi/8$ , while the amplitude transmission

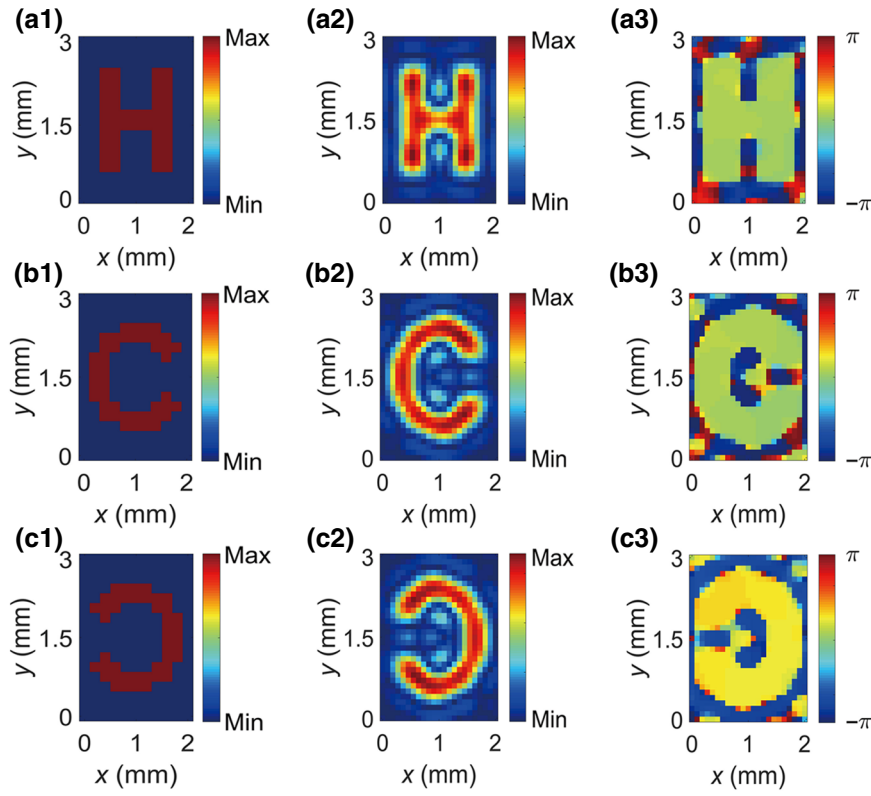


FIG. 3. Calculation results for three letter patterns by the SA algorithm. (a1)–(c1) Preset images of letters “H,” “C,” and mirror image of letter “C.” (a2)–(c2) Amplitudes of these three patterns calculated by the SA algorithm. (a3)–(c3) Corresponding phase distributions of three patterns calculated based on the SA algorithm.

is maintained around 0.25 at the operating frequency of 0.8 THz, as shown in Fig. 2(c). The parameters of antennas and modulation results are obtained by using a commercial simulation software from FDTD Solutions based on the finite-difference time-domain (FDTD) method. In the simulation, the antenna unit shown in Fig. 2(b) is built as the model. We use the LCP (RCP) light to illuminate the rod slot antennas and get the transmitted RCP (LCP) field.

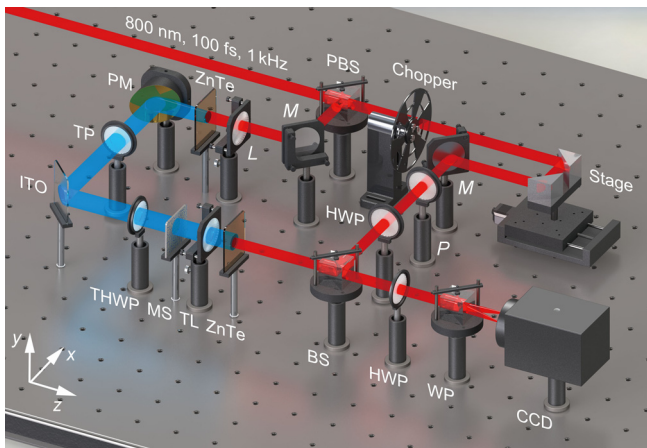


FIG. 4. Schematic of the experimental setup. PBS, polarized beam splitter;  $M$ , mirror;  $L$ , lens; PM, parabolic mirror; TP, THz polarizer; THWP, THz half-wave-plate; MS, metasurface sample; TL, THz lens;  $P$ , polarizer; HWP, half-wave-plate; BS, beam splitter; WP, Wollaston prism; CCD: charge-coupled device.

Similarly, the transmitted  $y$ -polarized ( $x$ -polarized) field from the C-shaped slot antennas can be obtained upon illumination of the  $x$ -polarized ( $y$ -polarized) light. The sample consisting of  $100 \times 100$  basic antenna units with a total dimension of  $1 \times 1 \text{ cm}^2$  is fabricated by using standard photolithography, film deposition, and a lift-off process. The image of part of the sample [see Fig. 2(d)] shows that both antenna arrays are well fabricated.

The simulated annealing (SA) algorithm is used to calculate the phase distributions of the holograms for these letter patterns, and then the phase distributions are employed to arrange each basic antenna [32]. In the SA algorithm, the exponential temperature curve is set as

$$t(k) = t_0 \times a^k, \quad (3)$$

where  $t_0$  is the initial temperature, which is set as 0.1,  $q$  is the iteration number, and  $a$  is the cooling temperature ratio, which is set as 0.99 in the optimization. In each iteration, the discrete Fraunhofer diffraction integral is used to calculate the optical field  $U_2(m_2, n_2)$  on the image plane from the optical field  $U_1(m_1, n_1)$  on the source plane

$$U_2(m_2, n_2) = \sum_{m_1=1}^M \sum_{n_1=1}^N Gx(m_2, m_1)U_1(m_1, n_1)G'_y(n_2, n_1), \quad (4)$$

where  $m_1, n_1$  ( $m_2, n_2$ ) are the subscripts of the discrete optical field matrix  $U_1$  ( $U_2$ ) and  $M \times N$  is the size of  $U_1$ ,

which is  $50 \times 50$  in our case.  $G_x(m_2, m_1)$  and  $G_y(n_2, n_1)$  are the discrete Fraunhofer transform matrices, which can be expressed as

$$G_x(m_2, m_1) = \frac{e^{jkf}}{\sqrt{j\lambda f}} \exp\left(\frac{-jk}{f} m_2 \delta_2 \cdot m_1 \delta_1\right), \quad (5)$$

$$G_y(n_2, n_1) = \frac{e^{jkf}}{\sqrt{j\lambda f}} \exp\left(\frac{-jk}{f} n_2 \delta_2 \cdot n_1 \delta_1\right), \quad (6)$$

where  $f$  is the focal length of the Fourier lens and is set as 10 mm.  $\delta_1$  and  $\delta_2$  are the pixel sizes on the source plane and image plane, respectively. After 2500 iterations, we get stable and high-quality holographic images, as shown in Fig. 3. The width and height of each pattern are 2 and 3 mm, respectively. The calculated amplitude and phase distributions of all three patterns are acceptable and the signal-to-noise ratio is high enough. The difference between the preset and calculated images is attributed to the limited pixel numbers, which are  $50 \times 50$  for the source plane due to the limited size of the THz beam.

### III. RESULTS AND DISCUSSION

A THz focal plane imaging system [33,34] is used to characterize the performance of the designed structure. The experimental set-up is shown in Fig. 4. A Ti:sapphire regenerative amplifier is used to produce a 100-fs ultra-short laser pulse with a spot diameter of 8 mm, a central

wavelength of 800 nm, and a repetition rate of 1 kHz. The laser beam with an average power of 900 mW is divided into two parts, which are then used as the pump (880 mW) and probe (20 mW) beams for the generation and detection of the THz waves, respectively. The pump beam impinges on a 1-mm-thick  $\langle 110 \rangle$  ZnTe crystal to generate the THz beam via the optical rectification effect. The horizontally polarized ( $x$ -polarized) THz beam (diameter 24 mm) passes through a THz polarizer (TP) to maintain its polarization before impinging on the structure, and the scattered THz beam is detected using another  $\langle 110 \rangle$  ZnTe crystal. In the probe optical path, a half-wave plate (HWP) and a polarizer ( $P$ ) are used to modulate the probe beam polarization. In the sensor crystal, the polarization of the probe beam is modulated by the THz field via the Pockels effect, while the reflected probe beam is captured by the imaging unit. The Wollaston prism (WP) is used to split the probe beam into two beams with orthogonal polarizations, and the two images of the sensor crystal are then projected onto a CCD camera. The THz complex field is extracted using the balanced electro-optic detection technique. By varying the optical path difference between the THz beam and the probe beam, 100 temporal images are captured at each time delay within a time window of 17 ps. The amplitude and phase information at the different frequencies are extracted by performing Fourier transformations on the temporal signals that occur at each pixel. Finally, the linearly polarized THz fields are detected and expressed as:

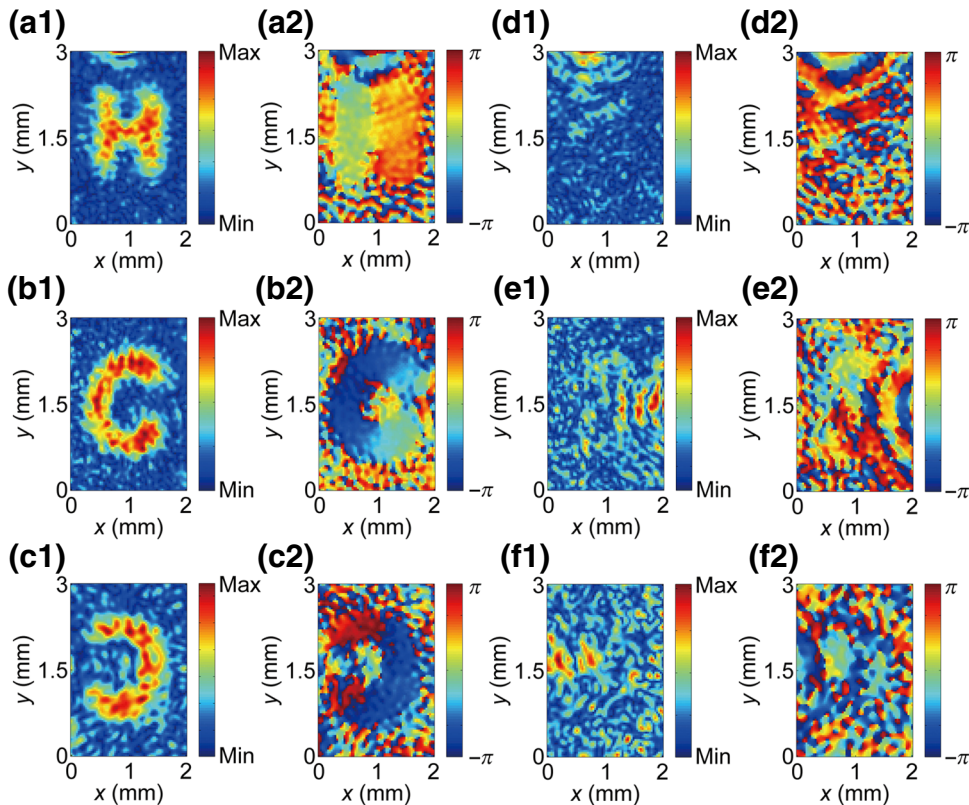


FIG. 5. Experimental results for each channel. (a1)–(c1) Amplitude distributions of the transmitted fields  $\mathbf{E}_{xy}$ ,  $\mathbf{E}_{RL}$ , and  $\mathbf{E}_{LR}$  in channels 1, 2, and 3, respectively. The first and second letters in subscript represent the incident polarization and detection polarization, respectively. (a2)–(c2) Corresponding phase distributions of  $\mathbf{E}_{xy}$ ,  $\mathbf{E}_{RL}$ , and  $\mathbf{E}_{LR}$ . (d1)–(f1) Amplitude distributions of the transmitted field  $\mathbf{E}_{LL}$  in channels 1, 2, and 3. (d2)–(f2) Corresponding phase distributions of  $\mathbf{E}_{LL}$ .

$\mathbf{E}_{xx}$ ,  $\mathbf{E}_{xy}$ ,  $\mathbf{E}_{yx}$ , and  $\mathbf{E}_{yy}$  at 0.8 THz. The first and second letters in the subscript represent the polarization state of the incident THz wave and that of the detection wave, respectively. All the circularly polarized fields can be derived based on Eq. (1).

First, we demonstrate the holographic images in each channel by selecting the polarization states of the incident and detection waves, that is, the holographic images can be revealed or not. The cross-polarized fields transmitted through the metasurfaces  $\mathbf{E}_{xy}$ ,  $\mathbf{E}_{RL}$ , and  $\mathbf{E}_{LR}$  are detected for channels 1, 2, and 3, respectively. The corresponding experimental results are shown in Fig. 5. Figures 5(a)–5(c) are the amplitude and phase distributions of the transmitted fields  $\mathbf{E}_{xy}$ ,  $\mathbf{E}_{RL}$ , and  $\mathbf{E}_{LR}$  for channels 1, 2, and 3, respectively. One can see that the images of letters are clearly extracted in each channel. If we change the polarization

states of the incident and detection waves to the same circular polarization, such as  $\mathbf{E}_{LL}$  or  $\mathbf{E}_{RR}$ , no images can be detected in all three channels. Figures 5(d)–5(f) present the amplitude and phase distributions of  $\mathbf{E}_{LL}$  in channels 1, 2, and 3, respectively. There are no images at all and the speckles in the figures are the crosstalk caused by the focused  $\mathbf{E}_{LL}$  on the center of the imaging area. This unambiguously shows that the images can be encoded into three channels through the designed metasurface and we can choose the image information in different channels by selecting the polarizations of incident and detection waves.

The metasurface can also realize optical hiding and verification in multiple channels. First, we demonstrate two-channel hiding and verification by properly choosing the polarizations of incident and detection waves. The corresponding experimental results are shown in Fig. 6.

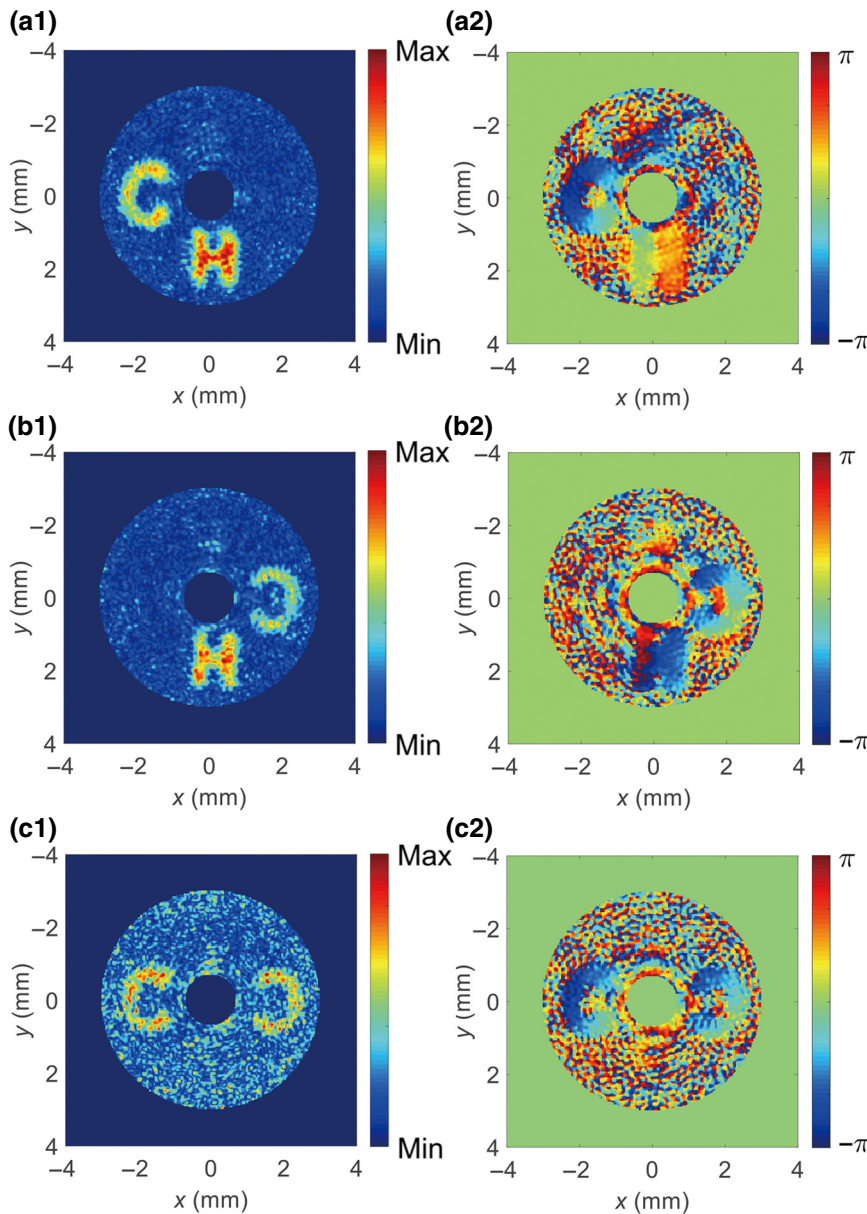


FIG. 6. Experimental results for two-channel characterization. (a1)–(a2) Amplitude and phase distributions of the transmitted field  $\mathbf{E}_{Rx}$ . The letters in channels 1 and 2 are detected. (b1)–(b2) Amplitude and phase distributions of the transmitted field  $\mathbf{E}_{Lx}$ . The letters in channels 1 and 3 are detected. (c1)–(c2) Amplitude and phase distributions of the transmitted field  $\mathbf{E}_{xx}$ . The letters in channels 2 and 3 are detected.

Figures 6(a1) and 6(a2) describe the amplitude and phase distributions of field  $\mathbf{E}_{Rx}$ , where both images in channels 1 and 2 have been detected. Figures 6(b1) and 6(b2) present the amplitude and phase distributions of the field  $\mathbf{E}_{Lx}$ , where the images hidden in channels 1 and 3 can be detected. Figures 6(c1) and 6(c2) present the amplitude and phase distributions of the field  $\mathbf{E}_{xx}$ , where the images hidden in channels 2 and 3 can be detected. The unconverted light is focused on the center of the image area, which has been removed for better observation.

Then, we demonstrate the results of optical image identification in three channels, as shown in Fig. 7. Figures 7(a1) and 7(a2) are the amplitude and phase distributions of  $\mathbf{E}_{xy}$ , where all three patterns can be observed. Figures 7(b1) and 7(b2) are the amplitude and phase distributions of  $\mathbf{E}_{RR}$ , which are the same as those of  $\mathbf{E}_{LL}$ , where only the apparent focal spot in the center of the imaging area is observed.

All possible results for different polarization combinations of incident and detection waves are shown in Table I. It is worth mentioning that only channel 2 or channel 3 appears in the  $\mathbf{E}_{RL}$  or  $\mathbf{E}_{LR}$  situations, and channel 1 disappears in these situations. We employ  $\mathbf{E}_{RL}$  to explain this phenomenon. According to Eq. (1), the incident right circular polarized field can be expressed as

$$\mathbf{E}_{Rin} = \frac{1}{\sqrt{2}}(\mathbf{E}_{xin} + j\mathbf{E}_{yin}), \quad (7)$$

where  $\mathbf{E}_{xin}$  and  $\mathbf{E}_{yin}$  have the same values. Then the  $\mathbf{E}_{xin}$  and  $\mathbf{E}_{yin}$  will be converted into the light beam with cross polarization by the C-shaped slot antennas with a conversion efficiency  $\eta$  (approximately 20% in our simulation). The detected  $x$ - and  $y$ -polarization components can be expressed as

$$\begin{aligned} \mathbf{E}_{xout} &= \eta j \mathbf{E}_{yin}, \\ \mathbf{E}_{yout} &= \eta \mathbf{E}_{xin}. \end{aligned} \quad (8)$$

Thus, the output left circularly polarized  $\mathbf{E}_{Lout}$  field can be obtained as

$$\mathbf{E}_{Lout} = \frac{1}{\sqrt{2}}(\mathbf{E}_{xout} - j\mathbf{E}_{yout}) = \frac{1}{\sqrt{2}}(\eta j \mathbf{E}_{yin} - j \eta \mathbf{E}_{xin}). \quad (9)$$

Since the amplitudes of  $\mathbf{E}_{xin}$  and  $\mathbf{E}_{yin}$  are the same, the output  $\mathbf{E}_{Lout}$  field should be 0, meaning there is no image in channel 1. However, the image converted by the rod slot antennas will appear in channel 2. For the case of  $\mathbf{E}_{LR}$ , there is an image in channel 3, but no image is observed in channel 1, as shown in Table I. For the  $\mathbf{E}_{xy}$  or  $\mathbf{E}_{yx}$  situation,  $\mathbf{E}_{xy}$  or  $\mathbf{E}_{yx}$  will generate an image in channel 1 and the  $\mathbf{E}_{RL}$  and  $\mathbf{E}_{LR}$  will generate an image in channels 2 and 3, respectively, thus we can observe all three images (shown in Table I and Fig. 7).

Compared to other polarization-sensitive metasurfaces consisting of one type of antenna, the combined structures

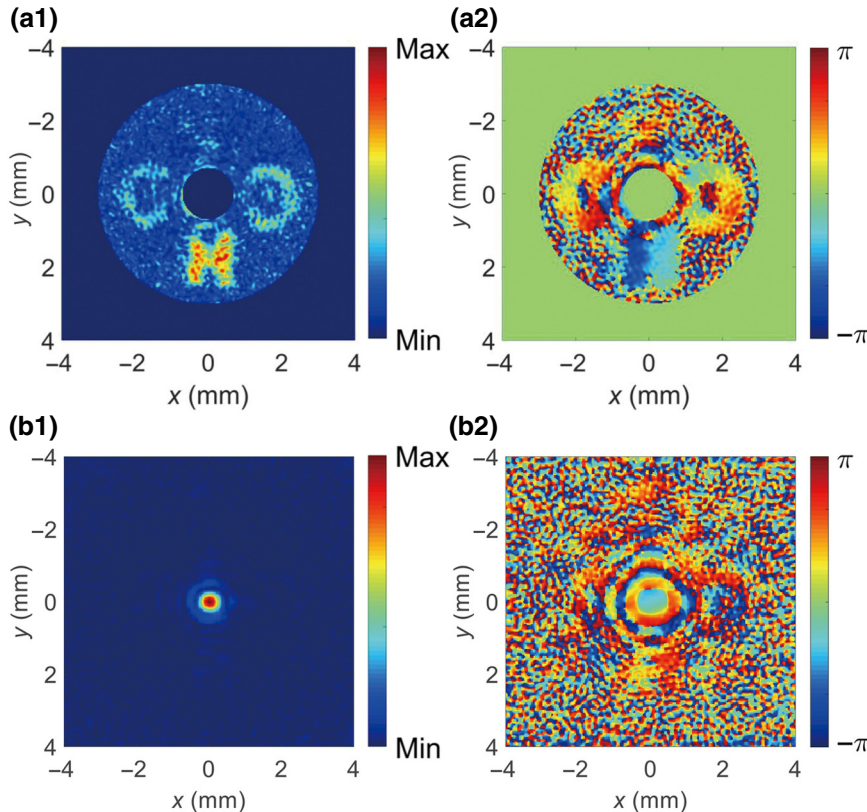


FIG. 7. Experimental results for three-channel characterization. (a1)–(b1) Amplitude and phase distributions of transmitted field  $\mathbf{E}_{xy}$ . The letters in channels 1, 2, and 3 are detected. (b1)–(b2) Amplitude and phase distributions of the transmitted field  $\mathbf{E}_{RR}$ . None of three channels is detected.

TABLE I. All possible measured results.

	<i>x</i> -pol. <sup>a</sup>	<i>y</i> -pol.	LCP	RCP
<i>x</i> -pol. <sup>b</sup>	2, 3 <sup>c</sup>	1, 2, 3	1, 2	1, 3
<i>y</i> -pol.	1, 2, 3	2, 3	1, 2	1, 3
LCP	1, 3	1, 3	None	3
RCP	1, 2	1, 2	2	None

<sup>a</sup>This row represents the polarization state of the detection wave.

<sup>b</sup>This column represents the polarization state of the incident wave.

<sup>c</sup>The number represents which channel can be detected.

can provide more channels based on the polarization control [35–38]. The combination of two types of antennas increases the number of channels to three without introducing a new physical dimension, dramatically increasing the transmission information capability of the metasurface structure. Benefiting from the combined structure, there are a total of seven different results obtained by adjusting the polarization states of both incident and detection waves. Moreover, the capacity of the proposed approach can be further enhanced by combing other multiplexing techniques, such as wavelength [39,40], position [15], and orbital angular momentum [24]. For example, if the metasurface can work for both linear and circular polarized light for two different wavelengths, 14 different results can be achieved by a single metasurface device.

#### IV. CONCLUSIONS

We experimentally demonstrate a polarization multiplexed metasurface hologram based on the simultaneous control of the linear and circular polarizations. The developed metasurface device has three operation channels to deliver the optical information. Three holographic images are reconstructed in different channels. By controlling the polarization states of the incident and detection waves, the optical images encoded in these three channels are selectively extracted. This multi-image hiding and verification approach will benefit the identification system. The feasibility study of our work shows that the proposed approach can add alternative degrees of freedom for the polarization controlled metasurface, namely, it can simultaneously modulate two basic polarization states in a single metasurface. This design method increases the communication channel of the device without introducing any new physical dimension, which can greatly increase the functionality density of the integrated device and find alternative applications in the fields of optical image encoding and security of optical information.

#### ACKNOWLEDGMENTS

This work was supported by the National Natural Science Foundation of China (Grants No. 11774243,

No. 11774246, No. 11404224, and No. 11474206); Youth Innovative Research Team of Capital Normal University (Grant No. 008/19530050146); Beijing Youth Top-Notch Talent Training Plan (Grant No. CIT&TCD 201504080); Capacity Building for Science and Technology Innovation—Fundamental Scientific Research Funds (Grants No. 008/19530050170, No. 008/19530050180, No. 008/18530500186, and No. 025185305000/142); Beijing Talents Project (Grant No. 2018A19); Scientific Research Base Development Program of the Beijing Municipal Commission of Education. X.C. acknowledges the Engineering and Physical Sciences Research Council of the United Kingdom (Grant No. EP/P029892/1).

H.Z. and C.Z. contributed equally to this work.

- [1] C. M. Zhang, D. D. Wen, F. Y. Yue, Y. Intaravanne, W. Wang, and X. Z. Chen, Optical Metasurface Generated Vector Beam for Anticounterfeiting, *Phys. Rev. Appl.* **10**, 034028 (2018).
- [2] F. Y. Yue, C. M. Zhang, X. F. Zang, D. D. Wen, B. D. Gerardot, S. Zhang, and X. Z. Chen, High-resolution gray scale image hidden in a laser beam, *Light Sci. Appl.* **7**, e17129 (2018).
- [3] N. F. Yu, P. Genevet, M. A. Kats, F. Aieta, J. P. Tetienne, F. Capasso, and Z. Gaburro, Light propagation with phase discontinuities: generalized laws of reflection and refraction, *Science* **334**, 333 (2011).
- [4] F. Aieta, P. Genevet, M. A. Kats, N. F. Yu, R. Blanchard, Z. Gaburro, and F. Capasso, Aberration-free ultrathin flat lenses and axicons at telecom wavelengths based on plasmonic metasurfaces, *Nano. Lett.* **12**, 4932 (2012).
- [5] N. F. Yu, F. Aieta, P. Genevet, M. A. Kats, Z. Gaburro, and F. Capasso, A broadband, background-free quarter-wave plate based on plasmonic metasurfaces, *Nano. Lett.* **12**, 6328 (2012).
- [6] X. J. Ni, N. K. Emani, A. V. Kildishev, A. Boltasseva, and V. M. Shalaev, Broadband light bending with plasmonic nanoantennas, *Science* **335**, 427 (2012).
- [7] M. A. Kats, P. Genevet, G. Aoust, N. F. Yu, R. Blanchard, F. Aieta, Z. Gaburro, and F. Capasso, Giant birefringence in optical antenna arrays with widely tailorable optical anisotropy, *Proc. Natl. Acad. Sci. U. S. A.* **109**, 12364 (2012).
- [8] X. B. Yin, Z. L. Ye, J. Rho, Y. Wang, and X. Zhang, Photonic spin hall effect at metasurfaces, *Science* **339**, 1405 (2013).
- [9] J. F. Wang, S. B. Qu, H. Ma, Z. Xu, A. X. Zhang, H. Zhou, H. Y. Chen, and Y. F. Li, High-efficiency spoof plasmon polariton coupler mediated by gradient metasurfaces, *Appl. Phys. Lett.* **101**, 201104 (2012).
- [10] S. Larouche, Y. J. Tsai, T. Tyler, N. M. Jokerst, and D. R. Smith, Infrared metamaterial phase holograms, *Nat. Mater.* **11**, 450 (2012).
- [11] X. Ni, A. V. Kildishev, and V. M. Shalaev, Metasurface hologram for visible light, *Nat. Commun.* **4**, 2807 (2007).



- [12] D. Hu, X. K. Wang, S. F. Feng, J. S. Ye, W. F. Sun, Q. Kan, P. J. Klar, and Y. Zhang, Ultrathin terahertz planar elements, *Adv. Opt. Mater.* **1**, 186 (2013).
- [13] X. Q. Zhang, Z. Tian, W. S. Yue, J. Q. Gu, S. Zhang, J. G. Han, and W. L. Zhang, Broadband terahertz wave deflection based on C-shape complex metamaterials with phase discontinuities, *Adv. Mater.* **25**, 4566 (2013).
- [14] Y. Zhao and A. Alù, Manipulating light polarization with ultrathin plasmonic metasurfaces, *Phys. Rev. B* **84**, 205428 (2011).
- [15] M. Q. Mehmood, S. Mei, S. Hussain, K. Huang, S. Y. Siew, L. Zhang, T. Zhang, X. Ling, H. Liu, J. Teng, A. Danner, S. Zhang, C. W. Qiu, Visible-frequency metasurface for structuring and spatially multiplexing optical vortices, *Adv. Mater.* **28**, 2533 (2016).
- [16] H. O. Moser, L. K. Jian, H. S. Chen, M. Bahou, S. M. Kalaiselvi, S. Virasawmy, S. M. Maniam, X. X. Cheng, S. P. Heussler, S. bin Mahmood, B. I. Wu, All-metal self-supported THz metamaterial – the meta-foil, *Opt. Express* **17**, 23914 (2009).
- [17] H. O. Moser and C. Rockstuhl, 3D THz metamaterials from micro/nanomanufacturing, *Laser Photonics Rev.* **6**, 219 (2012).
- [18] J. F. Wu, B. H. Ng, H. D. Liang, M. B. H. Breese, M. H. Hong, S. A. Maier, H. O. Moser, and O. Hess, Chiral Meta-Foils for Terahertz Broadband High-Contrast Flexible Circular Polarizers, *Phys. Rev. Appl.* **2**, 014005 (2014).
- [19] J. F. Wu, H. O. Moser, S. Xu, A. Banas, K. Banas, H. S. Chen, and M. B. H. Breese, From polarization-dependent to polarization-independent THz meta-foils, *Appl. Phys. Lett.* **103**, 191114 (2013).
- [20] X. Z. Chen, M. Chen, M. Q. Mehmood, D. D. Wen, F. Y. Yue, C. W. Qiu, and S. Zhang, Longitudinal multifoci metalens for circularly polarized light, *Adv. Opt. Mater.* **3**, 1201 (2015).
- [21] D. Wintz, P. Genevet, A. Ambrosio, A. Woolf, and F. Capasso, Holographic metalens for switchable focusing of surface plasmons, *Nano Lett.* **15**, 3585 (2015).
- [22] L. L. Huang, X. Z. Chen, B. F. Bai, Q. F. Tan, G. F. Jin, T. Zentgraf, and S. Zhang, Helicity dependent directional surface plasmon polariton excitation using a metasurface with interfacial phase discontinuity, *Light Sci. Appl.* **2**, e70 (2013).
- [23] J. P. Liu, C. J. Min, T. Lei, L. P. Du, Y. S. Yuan, S. B. Wei, Y. P. Wang, and X. C. Yuan, Generation and detection of broadband multi-channel orbital angular momentum by micrometer-scale meta-reflectarray, *Opt. Express* **24**, 212 (2016).
- [24] F. Y. Yue, D. D. Wen, C. M. Zhang, B. D. Gerardot, W. Wang, S. Zhang, and X. Z. Chen, Multichannel polarization-controllable superpositions of orbital angular momentum states, *Adv. Mater.* **29**, 1603838 (2017).
- [25] J. W. He, X. K. Wang, D. Hu, J. S. Ye, S. F. Feng, Q. Kan, and Y. Zhang, Generation and evolution of the terahertz vortex beam, *Opt. Express* **21**, 20230 (2013).
- [26] W. T. Chen, K.-Y. Yang, C.-M. Wang, Y.-W. Huang, G. Sun, I.-D. Chiang, C. Y. Liao, W.-L. Hsu, H. T. Lin, S. Sun, L. Zhou, A. Q. Liu, D. P. Tsai, High-efficiency broadband meta-hologram with polarization-controlled dual images, *Nano Lett.* **14**, 225 (2014).
- [27] Q. Wang, X. Zhang, E. Plum, Q. Xu, M. Wei, Y. Xu, H. Zhang, Y. Liao, J. Gu, J. Han, and W. Zhang, Polarization and frequency multiplexed terahertz meta-holography, *Adv. Opt. Mater.* **5**, 1700277 (2017).
- [28] Y. W. Huang, W. T. Chen, W. Y. Tsai, P. C. Wu, C. M. Wang, G. Sun, and D. P. Tsai, Aluminum plasmonic multicolor meta-hologram, *Nano Lett.* **15**, 3122 (2015).
- [29] W. M. Ye, F. Zeuner, X. Li, B. Reineke, S. He, C. W. Qiu, J. Liu, Y. T. Wang, S. Zhang, and T. Zentgraf, Spin and wavelength multiplexed nonlinear metasurface holography, *Nat. Commun.* **7**, 11930 (2016).
- [30] C. M. Zhang, F. Y. Yue, D. D. Wen, M. Chen, Z. R. Zhang, W. Wang, and X. Z. Chen, Multichannel metasurface for simultaneous control of holograms and twisted light beams, *ACS Photonics* **4**, 1906 (2017).
- [31] L. L. Liu, X. Q. Zhang, M. Kenney, X. Q. Su, N. N. Xu, C. M. Ouyang, Y. L. Shi, J. G. Han, W. L. Zhang, and S. Zhang, Broadband metasurfaces with simultaneous control of phase and amplitude, *Adv. Mater.* **26**, 5031 (2014).
- [32] Q. F. Zhu, D. Y. Wang, X. H. Zheng, and Y. Zhang, Optical lens design based on metallic nanoslits with variant widths, *Appl. Opt.* **50**, 1879 (2011).
- [33] X. K. Wang, Y. Cui, W. F. Sun, J. S. Ye, and Y. Zhang, Terahertz polarization real-time imaging based on balanced electro-optic detection, *J. Opt. Soc. Am. A* **27**, 2387 (2010).
- [34] X. K. Wang, Y. Cui, W. F. Sun, J. S. Ye, and Y. Zhang, Terahertz real-time imaging with balanced electro-optic detection, *Opt. Commun.* **283**, 4626 (2010).
- [35] F. Walter, G. X. Li, C. Meier, S. Zhang, and T. Zentgraf, Ultrathin nonlinear metasurface for optical image encoding, *Nano Lett.* **17**, 3171 (2017).
- [36] J. X. Li, S. Kamin, G. X. Zheng, F. Neubrech, S. Zhang, and N. Liu, Addressable metasurfaces for dynamic holography and optical information encryption, *Sci. Adv.* **4**, eaar6768 (2018).
- [37] L. L. Li, T. J. Cui, W. Ji, S. Liu, J. Ding, X. Wan, Y. B. Li, M. H. Jiang, C. W. Qiu, and S. Zhang, Electromagnetic reprogrammable coding-metasurface holograms, *Nat. Commun.* **8**, 197 (2017).
- [38] X. F. Zang, F. Dong, F. Yue, C. Zhang, L. Xu, Z. Song, M. Chen, P.-Y. Chen, G. S. Buller, Y. Zhu, S. Zhuang, W. Chu, S. Zhang, X. Chen, Polarization encoded color image embedded in a dielectric metasurface, *Adv. Mater.* **30**, 1707499 (2018).
- [39] X. H. Zhang, M. B. Pu, X. Li, P. Gao, X. L. Ma, C. T. Wang, and X. G. Luo, Helicity multiplexed spin-orbit interaction in metasurface for colorized and encrypted holographic display, *Ann. Phys.* **529**, 1700248 (2017).
- [40] F. L. Dong, H. Feng, L. Xu, B. Wang, Z. Song, X. Zhang, L. Yan, X. Li, Y. Tian, W. Wang, L. Sun, Y. Li, W. Chu, Information encoding with optical dielectric metasurface via independent multichannels, *ACS Photonics* **6**, 230 (2019).